

REPORT DOCUMENTATION PAGE				Form Approved OMB No. 0704-0188	
Public reporting burden for this collection of information is estimated to average 1 hour per response, including the time for reviewing instructions, searching existing data sources, gathering and maintaining the data needed, and completing and reviewing this collection of information. Send comments regarding this burden estimate or any other aspect of this collection of information, including suggestions for reducing this burden to Department of Defense, Washington Headquarters Services, Directorate for Information Operations and Reports (0704-0188), 1215 Jefferson Davis Highway, Suite 1204, Arlington, VA 22202-4302. Respondents should be aware that notwithstanding any other provision of law, no person shall be subject to any penalty for failing to comply with a collection of information if it does not display a currently valid OMB control number. PLEASE DO NOT RETURN YOUR FORM TO THE ABOVE ADDRESS.					
1. REPORT DATE (DD-MM-YYYY) 27-02-2012		2. REPORT TYPE Final Technical		3. DATES COVERED (From - To) 1-Mar-09 to 30-Nov-11	
4. TITLE AND SUBTITLE (U) Collaborative Research: Advanced Excimer Laser Measurements and LES Modeling of Supersonic Combustion				5a. CONTRACT NUMBER	
				5b. GRANT NUMBER FA9550-09-1-0205	
				5c. PROGRAM ELEMENT NUMBER 61102F	
6. AUTHOR(S) Robert W. Pitz				5d. PROJECT NUMBER 2308	
				5e. TASK NUMBER BX	
				5f. WORK UNIT NUMBER	
7. PERFORMING ORGANIZATION NAME(S) AND ADDRESS(ES) Vanderbilt University Office of Sponsored Programs 1400 18th Ave. South (Sony building) Nashville, TN 37212-2809				8. PERFORMING ORGANIZATION REPORT NUMBER	
9. SPONSORING / MONITORING AGENCY NAME(S) AND ADDRESS(ES) Air Force Office of Scientific Research 875 North Randolph Street Suite 325, Room 3112 Arlington VA 22203-1768				10. SPONSOR/MONITOR'S ACRONYM(S)	
				11. SPONSOR/MONITOR'S REPORT NUMBER(S) AFRL-OSR-VA-TR-2012-0389	
12. DISTRIBUTION / AVAILABILITY STATEMENT Approved for public release. Distribution is unlimited.					
13. SUPPLEMENTARY NOTES					
14. ABSTRACT Accurate numerical predictions are essential to the design of scramjet combustors, and in order to develop and properly validate these predictions accurate temperature, species concentration, and velocity measurements must be obtained. Large eddy simulation (LES) promises to give improved predictions of turbulent, supersonic combustion relative to CFD RANS models, and therefore, a LES approach employing a subgrid turbulent mixing model was selected to model both reacting and non-reacting flow in a cavity-stabilized supersonic combustor. Hydroxyl tagging velocimetry (HTV) measurements were made in a non-reacting Mach 2 air flow over the cavity with and without an upstream strut. Velocity profiles were compared to LES simulations with good agreement in both configurations. In the flow with an upstream strut, there were some model-data discrepancies in the strut wake region where better resolution of the shear layer – compression wave interactions were needed. UV Raman scattering was used to obtain temperature and major species concentrations in a Mach 2 flow over a cavity fueled with a 30% H ₂ /70% CH ₄ mixture. UV laser-induced fluorescence obscured the Raman spectra in rich regions but data was obtained in most of the cavity. The Raman composition and temperature data were in reasonable agreement with the LES simulations.					
15. SUBJECT TERMS					
16. SECURITY CLASSIFICATION OF:			17. LIMITATION OF ABSTRACT	18. NUMBER OF PAGES	19a. NAME OF RESPONSIBLE PERSON
a. REPORT	b. ABSTRACT	c. THIS PAGE			Chiping Li
Unclassified	Unclassified	Unclassified	UL	26	19b. TELEPHONE NUMBER (include area code) 703-696-8574

Collaborative Research:
**Advanced Excimer-Laser Measurements and LES Modeling of Supersonic
Combustion**

(Vanderbilt Grant/Contract Number: FA9550-09-1-0205)
(Georgia Tech Grant/Contract Number: FA9550-09-1-0370)
Prepared for:

Dr. Chiping Li,
Air Force Office of Scientific Research
Department of the Air Force (AFOSR/NA)
875 North Randolph Street, Room 732
Arlington, VA 22203-1977
(703) 696-8574 office
Chiping.li@afosr.af.mil

Submitted by

Robert W. Pitz, Professor
Department of Mechanical Engineering
Vanderbilt University
Nashville TN 37235
615-322-0209 office
615-343-8730 fax
pitzrw@vuse.vanderbilt.edu

and

Suresh Menon, Professor
School of Aerospace Engineering
Georgia Institute of Technology
270 Ferst Drive
Atlanta, GA 30332-0150
(404) 352-4740 office
suresh.menon@ae.gatech.edu

February 27, 2012

Executive Summary

Supersonic airflow over a wall cavity with a rear ramp both with and without an upstream strut is studied both experimentally with hydroxyl tagging velocimetry (HTV) and UV Raman scattering and numerically with large eddy simulation (LES). In the HTV experiments, an OH grid formed in a nonreacting airflow by crossing 11 lines by 11 lines is used to obtain velocities at ~120 grid points. The OH grid is tracked with a new template-matching method that determines both linear and rotational displacements. Mean and RMS fluctuation velocity profiles both with and without the strut are analyzed and compared to results obtained from LES simulations, and there is good overall agreement between the two methods. The experimental and LES results demonstrate that installing an upstream strut increased cavity recirculation along the centerline relative to the *no-strut* configuration. In addition, the shear layer is observed to grow more quickly and impinge higher on the ramp wall. Some disagreements are found in the measured and predicted propagation of the weak compression wake formed by the trailing edge of the strut and in the location of the velocity gradients in the cavity shear layer; possible reasons are identified and discussed for future study.

Having verified the accuracy of the LES simulation, experiments were then conducted in reacting flows over the same ramp close-out cavity without a strut using UV Raman scattering. The fuel, a mixture of 70% methane and 30% hydrogen, was chosen to approximate the reactivity of a JP-type fuel and to reduce the potential for formation of polycyclic aromatic hydrocarbons (PAH). Two cases are discussed: 1) with fuel injected from the cavity close-out ramp; 2) with additional air also injected from the close-out ramp. Raman signals were low as a result of low static pressure and measures taken to prevent damage to the test section windows. Furthermore, broadband interference in rich zones reduced the amount of usable data. Methane was observed to accumulate behind the step of the cavity, especially near the location of the shear layer. Higher temperatures and more complete combustion (overall) were observed when air was also injected into the cavity. LES simulations with a turbulent artificial neural network (TANN) is in reasonable agreement with the experimental values overall especially in the downstream portion of the cavity but with discrepancies in the upstream portion of the cavity. These differences may be caused by the broadband interference and resultant data biasing.

This grant helped support the following researchers at both Vanderbilt University and Georgia Tech:

Robert Pitz – Professor, Vanderbilt University

Nathan Grady – Ph.D. student (Completed M.S. Dec. 2010), Vanderbilt University

Jennifer Frankland – Undergraduate student, Vanderbilt University

Troy Friedlander – Undergraduate student, Vanderbilt University

Suresh Menon – Professor, Georgia Tech

Chaitanya Ghodke – M. S. (Graduated Dec. 2011), Georgia Tech

Jagannath Pranatharthikaran – M. S., Graduate student, Georgia Tech

This grant resulted in the following publications:

1. Grady, N. R., R. W. Pitz, C. D. Carter, K.-Y. Hsu, C. Ghodke, and S. Menon (2012) "Supersonic flow over a ramped-wall cavity flameholder with an upstream strut," *Journal of Propulsion and Power* (to appear).
2. El Baz, A.M. and R. W. Pitz (2011) " N_2O molecular tagging velocimetry", *Applied Physics B*, DOI 10.1007/s00340-012-4872-5.
3. Ramsey, M. C., and R. W. Pitz (2011), "Template matching for improved accuracy in molecular tagging velocimetry," *Experiments in Fluids*, **51**(3), 811-819.
4. Grady, N. R. (2010), "Hydroxyl tagging velocimetry in a supersonic flow over a ramped-wall cavity flameholder with an upstream strut," Master's Thesis, Vanderbilt University, Department of Mechanical Engineering, Nashville, TN.
5. Grady, N. R., J. H. Frankland, R. W. Pitz, C. D. Carter, and K.-Y. Hsu (2012), "UV Raman scattering measurements of supersonic reacting flow over a piloted, ramped cavity". AIAA-2012-614, 50th AIAA Aerospace Sciences Meeting, Nashville, Tennessee, January 9-13, 2012.
6. Grady, N. R., Friedlander, T., Pitz, R. W., Carter, C. D., and Hsu, K.-Y. (2010), "Hydroxyl tagging velocimetry in a supersonic flow over a piloted cavity," AIAA-20120-1405, 48th AIAA Aerospace Sciences Meeting, Orlando, Florida, January 4-7, 2010.
7. Ghodke, C., Choi, J., Srinivasan, S., Menon, S. (2011), "Large-Eddy Simulation of Supersonic Combustion in a Cavity-Strut Flameholder", AIAA-2011-323, 49th AIAA Aerospace Sciences Meeting, Orlando, FL, Jan 4-7, 2011.
8. Ghodke, C., Pranatharthikaran, J., Retaureau, R., Menon, S. (2011), "Numerical and Experimental Studies of Flame Stability in a Cavity Stabilized Hydrocarbon-Fueled Scramjet", 17th AIAA International Space Planes and Hypersonic Systems and Technologies Conference, San Francisco, California, April, 2011.
9. Choi, J., Ghodke, C., Menon, S. (2010), "Large-Eddy Simulation of Cavity Flame-Holding in a Mach 2.5 Cross Flow," AIAA-2010-414, 48th AIAA Aerospace Sciences Meeting, Orlando, Florida, Jan 4-7, 2010.

1.0 Project Description

1.1 Motivation

The current RANS CFD codes used to design scramjet combustors have simplified physics in order to calculate the complex geometry with detailed chemistry and unsteady compressible turbulent flow. However, while these models generally provide guidelines for future experimental efforts, they fail to capture the phenomenological flow patterns. Therefore, the use of large-eddy-simulations (LES), which promise to give improved prediction of turbulent combustion [1, 2] in supersonic combustion [3] have been proposed. LES simulations are more computationally efficient than direct numerical simulations (DNS) because they directly model only the large scale resolved features that contain the bulk of the kinetic energy and dominate the overall flow. The LES subgrid closure for the momentum and energy transport employs a transport model for the subgrid kinetic energy with specific corrections for compressible flow [3]. The scale-similar localized dynamic approach [4, 5] has been extended for compressible flow, and all model coefficients (including the turbulent Prandtl number) are obtained dynamically as part of the simulation.

How LES models small scale turbulent fluctuations and the use of either low or high order dissipation schemes is an important consideration for scramjet combustor modeling. While low dissipation schemes capture small scale turbulence well, they cannot capture shock waves adequately without the use of computationally prohibitive small grid size. To capture moving shocks and shear layer turbulence within the same simulation, the LES solver employs a hybrid algorithm [3, 6] that incorporates a high dissipation scheme in regions of strong discontinuities but switches locally and automatically to a low-dissipation scheme in regions of shear flow. The local switching is determined based on sensors that are sensitive to the pressure and density gradients in the flow and requires no user specific adjustments. While this approach has been shown to capture both shock and turbulence without requiring *ad hoc* adjustments in some flows, flows with complex/multiple interactions between shear layers and/or shocks can create errors [7]. These errors can be resolved either by increasing the grid resolution (which may be computationally expensive/prohibitive), or by optimizing the low-to-high dissipation switching (which may require additional experiments).

Further validation needs to be carried out for reacting flows with a robust subgrid closure of the small-scale turbulent fluctuations where the transfer of both internal energy and mass is important. Linear eddy mixing (LEM) is a means of providing subgrid scale closure for a LES cell without having to fix any constants such as turbulent Schmidt, Prandtl, or Lewis numbers. LEM makes dynamic evaluations of small-scale turbulent mixing coupled with molecular diffusion and reaction kinetics. A key challenge for applying LEM to turbulent mixing and combustion in supersonic flow is to allow for compressibility (and shock motion) in the small scales. Compressibility will affect turbulent mixing and also volumetric expansion due to heat release. Although a baseline LEM for supersonic combustion has been developed, to fully validate LEM or other subgrid scale closure schemes for compressible flow will require correctly predicting energy (both internal and kinetic) or species/mass dissipation as well as determining the velocity-scalar and scalar-scalar correlations. Therefore measurements of these scalar-velocity correlations are needed.

Most previous velocity measurements in supersonic flows have used particles to infer the gas velocity. In supersonic flows, particle drag effects can lead to significant errors in the velocity measurements [8]. Recently non-intrusive molecular velocity data has been obtained that can be compared to numerical models of supersonic flows. For example, measurements of

molecular velocity have been made in a generic scramjet combustor in Research Cell 19 at WPAFB in collaboration with AFRL researchers [7, 9-11] under non-reacting conditions. The velocity measurements were made with hydroxyl tagging velocimetry (HTV), a method developed at Vanderbilt University [12-16]. In the HTV method, an ArF excimer laser dissociates H_2O into OH to form an OH grid pattern in the flow. The OH grid formed at zero time is displaced by the flow and imaged at a fixed time delay. The displacement of the grid pattern over time delay determines the velocity pattern. HTV is a velocimetry technique with negligible particle drag and due to its linear dissociation of water can make a relatively large grid of velocity vectors.

In order to verify the chemistry of these numerical models, *in situ* and temporally resolved experimental measurements of temperature and species are needed. O'Byrne et al. [17] have performed extensive coherent anti-Stokes Raman scattering (CARS) measurements in a model scramjet combustor. They recorded temperature and mole fractions of O_2 , N_2 , and H_2 (employing vibrational CARS for O_2 and N_2 but rotational CARS for H_2) in a hydrogen-fueled scramjet duct; the approach used was a variant of the dual-pump CARS technique [18, 19]. Of course, in a hydrocarbon fueled combustor, measurement of all major species is a challenge for CARS. Spontaneous Raman scattering can satisfy this requirement (to measure all major species) and can also provide measurements along the length of the laser probe, a distinct advantage over CARS. For this research effort UV vibrational Raman scattering, based on a KrF excimer laser, with 248-nm excitation is employed; because scattering cross sections in the UV are significantly larger than scattering in the visible, single-shot scattering signals are relatively large (for the same laser pulse energy); a further advantage is that no pulse stretching is needed to avoid dielectric breakdown. A detailed description of Raman scattering is given by Barlow et al. [20]. UV Raman scattering has been used to measure temperature and chemical species concentrations in variety of combustion applications in "hostile environments" [21-23]; in particular, this approach has been used successfully in hydrogen supersonic jet flame [24].

Combined HTV and Raman can provide both the location of gradients, and quantitative data in the entire flow. Therefore, validation of both hybrid switching technique and the LEM method in both reacting and non-reacting flows can be obtained using the proposed experimental system. Additionally, the scalar-scalar and scalar-velocity correlation can be used to evaluate closures used in other LES methods (e.g., gradient diffusion and scalar dissipation based flamelet models). However, before such a combined system can be successfully implemented, separate tests on the viability of each technique in scramjet combustor environments were conducted.

1.2 Research Highlights

Velocity Comparisons in Scramjet Flows

The experiments were conducted at the supersonic flow facility in Research Cell 19 [25] at the Propulsion Directorate, Wright-Patterson Air Force Base. The wind tunnel employed a 2-D Mach-2 nozzle with an airflow rate ranging from 1.5 to 3 kg/s. The test section has a constant area 51×152 mm isolator with a constant width of 152 mm. The combustor diverges 2.5° along the bottom wall 7.6 cm ahead of the of the cavity leading edge. A schematic for the cavity can be found in Fig. 1 with a ramped cavity and a strut present. The strut is 25.4 mm in height, and the leading edge has an 18.5° wedge and is swept by 30° . The trailing edge is swept by 45° with a constant thickness of 6.4 mm and is flush with the step of the cavity. The strut protrudes 25.4 mm over the cavity due to these sweep angles, and tapers to an 18.5° wedge at the top (see

Figure 1 (b)). This strut geometry is used since “strut 2”, of similar geometry [26], created an optimal balance of mixing and flame propagation. To reduce flow losses and improve performance, the strut used in the current work has a smaller compression angle and is both narrower and shorter than “strut 2” used by Hsu et al. [26]. Note that the rectangular cavity ($D = 16.5$ mm, $L = 66$ mm) data mentioned here for comparison with the current data are from a previous effort using the same wind tunnel [11]. Fused-silica windows (Esco S1-UV) allow optical access to the test section. Compressed air ($T_0 = 590/560$ K, $P_0 = 410/210$ kPa) is expanded to Mach 2 conditions ($T = 330/310$ K, $P = 53/26$ kPa for the strut and no strut configuration respectively) and flows above the ramped cavity. The supply air is dry, and so water is added into the settling chamber to provide the moist flow needed for HTV.

A schematic of the HTV system is shown in Fig. 2. A Lambda Physik Compex 150 ArF excimer laser produced the 193 nm “write” beam used to create the hydroxyl molecular tags. The ArF laser beam (20 mm high \times 10 mm wide, 100 mJ/pulse, broadband, 1 nm bandwidth) is split by a 50/50 beam splitter, with one beam sent under the tunnel to allow beam access from both sides of the tunnel (to avoid beam clipping when probing close to the cavity step/ramp). Before entering the test section through the windows, each beam passed through “grid optics”, comprised of a 300 mm focal length (fl) cylindrical lens (25 mm \times 40 mm) and a stack of eleven, 300 mm fl cylindrical lenslets (20 mm wide \times 2 mm high) oriented 90° from each other. These grid optics formed 11 grid lines each (beam diameter ~ 0.15 mm at measurement zone), for a total of 121 grid intersections. Laser energy measured before the lenses for each of the 193 nm laser beams of the current work was 7.5 mJ and 6.5 mJ for the no-strut configuration and 4 mJ and 6 mJ for the strut configuration, respectively. The difference between the energy out of the laser and what reaches the tunnel is due to absorption of the broadband ArF 193 nm laser by atmospheric O₂. The Compex 150 can produce narrowband radiation and be tuned between O₂ transitions to mitigate absorption; however, degradation of the optical components in the laser prevented narrowband operation.

The position of the 11 \times 11 OH gridlines created by the “write” beam is determined by a “read” process via OH planar laser-induced fluorescence (PLIF). The “read” beam is created by a Spectra Physics GCR-170 Nd:YAG pumping a Lumonics HD300 Hyperdye dye laser. The dye laser output was then frequency doubled within an Inrad Autotracker III; the 282 nm beam was separated from the dye beam within an Inrad Prism Harmonic Separator. The final output of the “read” laser system was ~ 14 mJ/pulse at 282 nm. The laser was tuned to the Q₁(1) transition of the A² Σ^+ ($v'=1$) \leftarrow X² Π ($v''=0$) band; this transition provides the maximum fluorescence signal at room temperatures and below. To ensure that the 282 nm beam remained tuned to the aforementioned transition, a small portion of the beam was split off and directed over small methane-air flame; OH laser-induced fluorescence was detected with a photomultiplier tube (PMT) attached to a 0.1-m monochromator. The 282-nm beam was then directed to a photodiode (PD), so that the 282-nm beam energy could be monitored. Both PMT and PD signals were then displayed on an oscilloscope. Timing for both the Nd:YAG and ArF lasers (and the PIMAX camera) was controlled with SRS DG-535 digital delay generators. The standard deviation of the random shot-to-shot timing fluctuation between the two lasers was about $\sigma = 8$ ns (equaling about 0.8% and 0.4% for the respective 1 μ s and 2 μ s delay settings).

The 282 nm OH probe beam was first expanded by a -150 mm fl cylindrical lens then focused using a 1 m fl spherical lens. The sheet thickness at the measurement location was ~ 0.2 mm for the no-strut measurements. It was observed that the strut created an out-of-plane velocity component in its wake region; thus, the 282 nm sheet was expanded to a thickness of ~ 0.3 mm

by moving the 1 m fl spherical lens back ~ 275 mm. OH laser-induced fluorescence was recorded by a Roper Scientific PIMAX Superblue intensified CCD camera fitted with a 100 mm fl Cerco lens ($f/2.8$). A narrow band filter (LC-300-325-50 UV-B manufactured by Laser Components GmbH) was employed to block background scattering (from surfaces and particles) and isolate fluorescence from the OH A-X (1,1) and (0,0) bands in the 306-320 nm region. The camera's 512 \times 512 pixel array was binned 2 \times 2 to allow for a 10 Hz framing rate (to match the laser repetition rate). After binning each "super" pixel viewed a region of about 175 $\mu\text{m} \times 175 \mu\text{m}$. The camera was mounted above the tunnel; the fluorescence was directed into the camera using a UV enhanced Al mirror after having passed through a fused silica window on top of the test section. The PLIF field of view was 45 mm \times 45 mm. The camera and sheet optics (for both laser systems) were mounted on a large breadboard, which itself was mounted to a large 3-axis translation system. The optics directing the 193- and 282-nm beams to the breadboard were arranged such that the table and probe plane could be translated vertically. Provisions were also made to readily translate the probe sheets to different streamwise probe positions.

The post-processing method used in this study [27] is capable of finding grid intersections with sub-pixel accuracy. The code uses a template matching method with several linear and rotational degrees of freedom to best match each of the intersections in a given image. The Gaussian templates from the undelayed image are then compared with the templates from the delayed image to determine two linear (x , y) and two rotation (θ_1 , θ_2) Lagrangian displacements in the two template coordinate systems. The uncertainty in locating the intersection location is dependent on the signal-to-noise ratio (SNR) of the image. SNR values for this study were between 4 and 6 yielding a velocity measurement uncertainty of $<2\%$ for the freestream values (c.f. Figure 7 from ref. [27]). The rotational displacements are then used to approximate the spatial velocity derivatives. Having obtained all of these values in the template coordinate systems, they are then transformed into the global coordinate system. An interpolation method (cubic or Powell-Sabin) is used to obtain velocity profiles with sub-intersection resolution. With these interpolated velocity profiles, y -axis (vertical) vorticity can be derived. A schematic showing the initial OH grid positions with respect to the cavity for the no-strut configuration is shown in [Fig. 3](#).

For the ramped cavity with strut configuration, a strong out-of-plane velocity component present in the wake region of the strut required three adaptations to the no-strut experimental setup. First, the thickness of the 282 nm read sheet was increased to 0.3 mm by moving the 1 m fl spherical lens back about ~ 0.275 m. Second, typical delay times for grids taken in the wake region were reduced to 1 μs . Finally, the stagnation pressure was decreased, to increase the relative humidity and thus OH PLIF signal strength.

Large eddy simulation (LES) of the flow in the same experimental test facility is then carried out to compare the predictions with the measurements. The entire test facility (from the stagnation chamber to the outflow nozzle) is modeled for the conditions used in the experiments. This allows removal of any uncertainties in determining the inflow conditions to the cavity regions. The numerical method employs the well-established compressible LES methodology [3, 6, 28-31]. The LES subgrid closure for the momentum and energy transport employs a transport model for the subgrid kinetic energy with specific corrections for compressible flow [3]. The scale-similar localized dynamic approach [4, 32] has been extended for compressible flow, and all model coefficients (including the turbulent Prandtl number) are obtained dynamically as part of the simulation; details can be found in the cited papers.

To capture moving shocks and shear layer turbulence within the same simulation, the LES solver employs a hybrid algorithm [3, 6] that incorporates a MUSCL reconstruction based on the HLL Riemann solver in regions of strong discontinuities but switches locally and automatically to a low-dissipation central-type scheme in regions of shear flow. This approach has been shown to be robust and captures both shock and turbulence without requiring ad hoc adjustments. The local switching is determined based on “sensors” that are sensitive to the pressure and density gradients in the flow and requires no user specific adjustments. The overall scheme is second-order accurate in regions away from shocks and in time. All simulations are carried out using a MPI based multi-block solver that scales efficiently in massively parallel systems.

Two configurations, a baseline cavity and a cavity with a strut positioned upstream of the cavity, were analyzed and compared with some of the earlier data [33]. In this paper [33], a more careful assessment of the model predictions against the measured data is reported, which also included reprocessing the data in the same manner as done in the experiments. A grid independence study has been performed using a range of grids. A fine grid of 12.3 million ($275 \times 300 \times 150$) for the no-strut configuration and 12.2 million ($250 \times 325 \times 150$) for the strut configuration showed overall similar results compared with that from an intermediate grid of around 10.3 million ($275 \times 250 \times 150$, no-strut configuration) and 9.9 million ($250 \times 265 \times 150$, strut configuration), and hence the intermediate grid is employed for all simulations. The reference Reynolds number based on the mean inflow velocity of 750 m/s and the cavity height of 0.0165 m is 3.7×10^5 for the no-strut case and 2.0×10^5 for the strut case. In general, the resolution at these Reynolds numbers required to resolve shock/shear layer interactions is uncertain [34]. As discussed below, comparison with data suggests that in some regions more grid resolution may be necessary for better agreement, but the grid choice is considered reasonable for this initial assessment. For all grids, turbulent kinetic energy spectra collected in shear layer and strut wake recover reasonable inertial range scaling indicating appropriateness of these grids for LES. Clustering of grids in regions of high gradients of pressure and in the near-wall region and shear layers is employed within the limited constraints of the chosen grid density. In the test section, the near-wall boundary layer is resolved with over 50 grid points before the cavity entrance. The smallest cell in the wall normal direction is 0.0014 mm with resulting $y^+ \sim O(1)$. Since the full test facility is simulated, the inflow is computed from the stagnation conditions, and outflow is supersonic. No-slip, adiabatic boundaries are used at all the walls. Simulations are performed for duration of 6 flow-through times with a flow-through time of ~ 2 ms defined on the basis of the combustor length and flow speed measured at the test section inlet. The solution is time-averaged for the last 3-4 flow-through times to obtain the statistics for comparison with data.

The single-shot velocity vectors are averaged to give mean and RMS velocity data. An example of the interpolated velocity profiles shown alongside the corresponding numerical prediction taken behind the strut is shown in Fig. 4. A comparison between experimental and numerical results of mean and RMS streamwise velocity at the centerline locations are shown in Fig. 5 without the strut and in Fig. 6 with the strut. Using these results and those obtained by Lahr et al. [11], comparisons between a ramped and a rectangular cavity can be made. An increase in both recirculation and turbulence was observed over the ramp as opposed to over the step which should aid in mixing and flameholding. Also, an expansion wave forms over the step of the ramped cavity as opposed to a shock wave in the rectangular cavity. This difference is caused by how the shear layer propagates over the respective cavities. In the ramped cavity, the

shear layer curls into the cavity creating an expansion corner whereas in the rectangular cavity the shear layer grows into the main combustor flow creating a compression corner. Furthermore, the shear layer growth rate in the ramped cavity was roughly one third of that observed in the rectangular cavity (0.05 and 0.14 respectively). The RMS fluctuation values peaked in the shear layer and are higher in the cavity than in the freestream. Increased turbulence and recirculation values are observed over the ramp of the cavity compared to the step of a rectangular cavity, but are similar in the upstream portion of the respective cavities. It is also observed that the shear layer impinged deeper into the cavity and grew more slowly than with the rectangular cavity. Both of these would reduce the flame propagation under reacting conditions, which may require some means of increasing the flame propagation into the freestream if the combustor were to be scaled up in size. Comparison with the LES results show overall excellent agreement in the location of the shear layer and overall profiles. Some discrepancies are seen in the shear layer regions, but overall the agreement is considered acceptable.

The case with the upstream strut shows that there is an increase in the propagation of the cavity flow deep into the freestream of the combustor by a) moving the shear layer impingement higher on the ramp, and b) via entrainment behind the strut. Furthermore, an increase in cavity recirculation ± 5 mm off the centerline was observed as seen in Fig. 7 that extended above the step similar to results shown in the literature. Although there was overall agreement of the LES prediction with data, some discrepancies were observed in the strut wake region: the propagation of the compression wave formed behind the strut was slightly different, as was the location and velocity gradients within the cavity shear layer. These discrepancies are likely due to the overall grid resolution employed in multiple regions of shear flow (root and tip) as well as an inability of the hybrid solver to accurately identify and resolve the multiple compression-shear interactions (also due to limited grid quality in these regions). Future studies will address this issue with local grid refinement.

The interpolated velocity data was then used to calculate vorticity. An example of this process for data taken behind the strut is shown in Fig. 8 shown alongside numerical predictions. The apparent vortices seen in the experimental data is an artifact of the grid spacing. Both the experimental and the numerical results agree in both magnitude and direction of the vortices, demonstrating the accuracy of both the measurements and the modeling in this complicated flow region.

Due interference from super-equilibrium OH in the reacting regions as shown by Grady et al [35], there are currently no velocimetry data available for analysis or comparison with CFD results in reacting flows. This work to obtain accurate velocity measurements in a supersonic flow in Research Cell 19 at WPAFB shows that Vanderbilt investigators have effectively collaborated with researchers at Georgia Tech to obtain velocity data for comparison to supersonic numerical codes.

Species Concentration and Temperature Measurements in Scramjet Flows

These experiments were also conducted in Research Cell 19 with the exact same wind tunnel configuration used in the *no strut* velocimetry experiment. The tunnel supplied heated (via a natural-gas heat exchanger), compressed air ($T_0 = 590$ K, $P_0 = 415$ kPa) that was expanded to Mach 2 conditions at the isolator ($T = 330$ K, $P = 53$ kPa) and was further expanded due to the 2.5° expansion of the combustor at the test section ($T = 300$ K, $P = 39$ kPa). It should be noted that these wind-tunnel conditions relate, roughly, to a Mach-4 scramjet flight condition; however, the resulting static temperature in the cavity region, ~ 300 K, is much lower than at true

flight conditions. Facility limitations (seals, etc.) prevented use of higher, more realistic temperatures for this study. A 70% methane (CH_4), 30% hydrogen (H_2) fuel mixture and air (when applicable) were injected parallel to the cavity floor from the cavity close-out ramp from the locations shown in Fig. 9. This fuel mixture was intended to represent the reactivity of a JP-type hydrocarbon fuel but also to minimize fluorescence interference. In both test cases, 102 SLPM (standard liters per minute, referenced to 273 K and 1 standard atmosphere) of fuel was injected and in one case an additional 100 SLPM of secondary air was also injected directly into the cavity.

A narrowband Lambda Physik Compex 150 KrF excimer laser (350 mJ/pulse, 20 ns pulse length) produced 248 nm radiation that was used to excite the vibrational Raman transitions. The laser was tuned away from O_2 and OH LIF transitions to reduce interference with the Raman lines. In order to prevent damage to the fused-silica wind-tunnel windows, two 200-mm focal length, cylindrical lenses, oriented 90° from each other, were used to focus the 248 nm beam. Additionally, a thin film polarizer was placed before the lenses to reject any unpolarized laser light. The laser energy measured after the lenses was ~ 200 mJ/pulse. Using burn patterns, the probe size was measured to be 0.75 in the x direction and 1.5 mm in the y direction. Raman scattering was collected through the top wind-tunnel window, collimated, and then focused onto the entrance slit of a Horiba iHR320 spectrometer using two $f/4$ UV achromats, as shown in Fig. 10; a 6-mm-long region of the beam was imaged. An n-butyl acetate filter was placed before the entrance slit to block the Rayleigh scattering at 248 nm. Raman signals were recorded with a PIMAX Superblue ICCD camera at a 10 Hz frequency. The photocathode was gated at 200 ns, and to further reduce background noise, multichannel plate gating was also used. The optics directing the 248 nm beam to the test section were arranged such that the probe region could be translated vertically and axially via a movable breadboard translation table.

Bottom wall pressure measurements along the combustor centerline are shown in Fig. 11; the pressure measurements taken upstream of the cavity were 3-5 kPa lower at the centerline than those taken closer to the tunnel walls. The drop in pressure at the fourth data point, $x = 120.4$ cm, was observed in all experimental runs, indicative of flow separation after recompression. Pressure measurements on the cavity floor were found to fluctuate $<1\%$ during each data set as, so pressure was assumed to be constant during each data set. Therefore, the ideal gas law was invoked to determine the temperature using the calculated number densities of the major species using linear interpolation of the wall pressure measurements for each test location. Since the number densities are in turn a function of temperature, the temperature was determined via an iterative scheme until convergence of ± 5 K was met. The Raman temperatures in the freestream agree well with the isentropic temperature of 300 K. The RMS temperature values were 6.8% in the freestream, where the true variation in temperature is expected to be very small, and 32% in the cavity.

At 8 vertical locations, 200 shots were collected, starting above the cavity shear layer and ending at the lowest point in the cavity assessable before the beam was clipped by the tunnel side wall. After a single vertical sweep was completed, the probe region was then moved axially from the upstream to downstream edge of the cavity. Plots for reducible images, and time averaged values for temperature and major species concentrations are shown in Figs. 12-18 each comparing values for both the fueling conditions. These figures represent a 0.75 mm line segment taken 9.5 mm off the centerline. Reducible images are those that reached temperature convergence and could be analyzed for temperature and concentration data. Failure to reduce a particular image was generally caused by interference. An example of a spectrum with

interference is shown in Fig. 19 alongside a spectrum with minimal interference both taken at the same location during combustion with no secondary air injection. As can be seen from Figs. 13-15, there is an accumulation of CH₄ with little CO₂ at high temperatures. Furthermore, local recirculation near the step in the spanwise direction can effectively trap unreacted fuel increasing residence time and creating fuel rich pockets such as the ones observed here and in other studies [36, 37]. Therefore, it is suggested that this interference is from polycyclic aromatic hydrocarbons (PAH) formed from this rich region, although no test was performed to confirm this.

Hsu et al. [37] also observed a fuel rich zone behind the step of the cavity using ethylene (C₂H₄) fuel. However, Hsu et al. noticed that the cavity became leaner overall when air was also injected along with the fuel, which is contrary to the observation in this experiment shown in Fig. 13 where air injection did not appear to decrease the CH₄ accumulation near the step. This difference is presumably due to the differences in reactivity between CH₄ and C₂H₄ fuels. In spite of the similarity in the methane profiles, there were some differences observed with the insertion of secondary air. Higher temperatures and water concentrations can be seen in Fig. 15 and 16 with secondary air injection than without. Furthermore as seen in Figs. 17 and 18, there is consistently less O₂ and H₂ inside the cavity with secondary air injection than without. The trends seen in Figs. 14-18 are indicative of more thorough combustion with secondary air injection. Unlike the profiles for temperature and H₂, inspection of the CO₂ profiles in Fig. 14 does not show consistently higher CO₂ with secondary air injection. However, the apparent maximum CO₂ concentrations occur at different locations for the two fueling conditions. Around x = 2 cm and to lesser extent around x = 3.5 cm, the maximum CO₂ levels are consistently lower in the cavity without secondary air injection. Therefore, it is apparent that the combustion of the methane fuel has been moved closer to the shear layer with secondary air injection. In addition, broadband interference, higher temperatures and H₂ values were observed in the shear layer near x = 1 cm only with secondary air injection perhaps due to a higher heat release.

Mixture fraction results are shown in Fig. 20 defining mixture fraction using C, H, and O atoms as suggested by Bilger [38]:

$$\xi \stackrel{\text{def}}{=} \frac{2 Y_C/W_C + \frac{1}{2} Y_H/W_H + (Y_{O,2} - Y_O)/W_O}{2 Y_{C,1}/W_C + \frac{1}{2} Y_{H,1}/W_H + Y_{O,2}/W_O}$$

and the stoichiometric mixture fraction of the fuel is 0.0525. The majority of the cavity is especially rich in both cases, and secondary air injection did not seem to have a strong effect the mixture fraction. In fact, the data indicates that in general there is an increase in mixture fraction with secondary air injection. Whether this observation is caused by the interference and resultant data biasing, or by reduced air entrainment into the cavity due to the extra heat release is uncertain. In addition to the interference intermittency, the species found near the step were observed to fluctuate between reactants and products similar to the “dynamic features” observed by Hsu et al [37]. In order to either clarify our mixture fraction data or to adequately capture the dynamic features observed better measurements and/or comparisons to numerical models are required.

While this experiment was only a partial success in its own right, it has been demonstrated that single-shot Raman scattering measurements are possible in such hostile environments. However, alterations will be required to ensure higher measurement fidelity.

First, using a test section pressure of 1 atm or higher is recommended since the ~0.4 atm pressure used here affected the signal strength. Upgrading from 50 to 100 mm diameter achromats would also greatly increase the signal strength. The use of a broadband polarizer could attenuate the unpolarized fluorescence interference while having a minimal effect on the highly polarized Raman scattering. Further refinement of the 248 nm focusing optics would tighten the focal spot of the Raman system and increase the signal-to-noise of the measurements. Additionally, either diluting the fuel mixture with N_2 and/or increasing the amount of H_2 in the fuel will presumably reduce the level of interference.

Species Concentration and Temperature Model-Data Comparisons in Scramjet Flows

LES studies of the reacting case using a 4-step methane-hydrogen reaction kinetics is carried out for the experimentally studied test case. LES using a turbulent artificial neural network (TANN) [39] scheme has been shown in the past to provide reasonable predictions of the reacting problem. In the TANNLES approach, the subgrid LEM is used to develop a database for the turbulence-chemistry interacting field and an ANN is trained on this database. The TANN is used during the simulation to provide the filtered reaction rates for the species during the simulation as a function of the local species, subgrid Reynolds number and resolved scalar dissipation. TANNLES in contrast to full subgrid simulation using the LEM closure is substantially cheaper and therefore, offers an approach that could provide a cost-effective LES approach to study this type of complicated flow.

Results using this TANNLES approach are provided in Figs. 21-25 for the pure fueling condition (i.e. no secondary air). Reasonable agreement exists inside the cavity between the two data sets for the measured species and temperature although some differences are clearly seen. Fairly good agreement exists for the CO and CO_2 profiles shown in Figs. 23 and 24 especially in the downstream portion of the cavity but differ in the upstream portion of the cavity where the numerical simulation consistently predicted more carbon products. There is also reasonable agreement with the water vapor profiles as well, as shown in Fig. 25. The discrepancies in the upstream portion of the cavity may be caused by biasing of the experimental data, inaccuracies in the chemistry closure, or some combination thereof. Assuming the data biasing preferentially eliminated reacting data points with higher product concentrations, then a reduction in mean product concentrations would be expected.

There were more noticeable discrepancies between the two data sets inside and above the shear layer most notably in the temperature profile in Fig. 21 where the numerical simulations failed to predict the elevated temperatures observed above the shear layer. While data biasing could contribute to the differences observed inside the cavity, there was little to no data biasing outside of the cavity. Therefore, it is possible that either the TANN requires more training with the fuel mixture used in the experiment or this chemistry closure scheme is slightly insufficient to accurately capture the chemistry in this combustor configuration. However, LES comparisons to the secondary air injection case may be more conclusive since secondary air resulted in more substantial combustion in the shear layer. The LES with the LEM using the finite-rate kinetics directly in the subgrid is also another approach that can be used to revisit this discrepancy in the shear layer. Such studies are being reviewed and will be reported in the future.

The current comparisons have helped to indicate how the experimental data may have been biased as a result of the interference, and also to assess the accuracy of LES TANN chemistry closure technique. Future comparisons to LES models with more robust chemistry

closures will further the understanding of cavity combustion and also help fine-tune the TANN based subgrid closure for scramjet application.

2. Conclusion

HTV and UV Raman measurements inside a model scramjet combustor were compared to LES numerical simulations. In the velocity measurement comparisons, increased turbulence and recirculation values are observed over the ramp of the cavity compared to the step of a rectangular cavity, but are similar in the upstream portion of the respective cavities. It is also observed that the shear layer impinged deeper into the cavity and grew more slowly than with the rectangular cavity. Both of these would reduce the flame propagation under reacting conditions, which may require some means of increasing the flame propagation into the freestream if the combustor were to be scaled up in size. Comparison with the LES results show overall excellent agreement in the overall profiles. Some discrepancies are seen in the shear layer regions, but overall the agreement is considered acceptable.

The case with the upstream strut shows that there is an increase in the propagation of the cavity flow deep into the freestream of the combustor by a) moving the shear layer impingement higher on the ramp, and b) entrainment behind the strut. Furthermore, an increase in cavity recirculation ± 5 mm off the centerline was observed that extended above the step similar to results shown in the literature. Although there was overall agreement of the LES prediction with data, some discrepancies were observed in the strut wake region: the propagation of the compression wave formed behind the strut was slightly different, as was the location and velocity gradients within the cavity shear layer. These discrepancies are likely due to the overall grid resolution employed in multiple regions of shear flow (root and tip) as well as an inability of the hybrid solver to accurately identify and resolve the multiple compression-shear interactions (also due to limited grid resolution in these regions). Future studies will address this issue with local grid refinement.

UV Raman measurement comparisons are currently on-going, however preliminary results have demonstrated that the 4-step chemistry closure used in LES TANN simulations are overall fairly accurate but failed to predict the elevated temperatures observed above the shear layer. Therefore, numerical predictions using more robust chemistry-closure schemes will be used for future comparisons. Experimental results showed considerable CH_4 accumulation behind the cavity step even with secondary air injection. This pool of unreacting methane may have resulted in polycyclic aromatic hydrocarbons (PAH) thus creating the broadband interference observed in this region, but no test was conducted to prove that PAH was present in the cavity. Despite the similarities in the methane distributions, secondary air injection resulted in higher temperatures, more heat release, more thorough combustion throughout the cavity, and peaks in the CO_2 profiles were consistently closer to the shear layer. In addition, combustion inside the shear layer was observed with secondary air injection due to the higher heat release. Furthermore, mixture fraction calculations using the reducible data show an increase in mixture fraction with secondary air injection. Whether this is a result of data biasing or through reduced air entrainment into the cavity is still being studied and will be compared to future numerical results using the full LEMLES and also modified TANN closure.

3.0 References

[1] Pitsch, H., Desjardins, O., Balarac, G., and Ihme, M., 2008, "Large-eddy simulation of turbulent reacting flows," *Progress in Aerospace Sciences*, **44**(6), pp. 466-478.

- [2] Sheikhi, M. R. H., Drozda, T. G., Givi, P., Jaber, F. A., and Pope, S. B., 2005, "Large eddy simulation of a turbulent nonpremixed piloted methane jet flame (Sandia Flame D)," *Proceedings of the Combustion Institute*, **30**, pp. 549-556.
- [3] Genin, F., and Menon, S., 2010, "Simulation of turbulent mixing behind a strut injector in supersonic flow," *AIAA Journal*, **48**(3), pp. 526-539.
- [4] Kim, W.-W., and Menon, S., "A new dynamic one-equation subgrid model for large-eddy simulations," 33rd Aerospace Sciences Meeting, Reno, NV, January 9-12, 1995, AIAA-2011-323, 2011.
- [5] Kim, W.-W., and Menon, S., 1999, "An unsteady incompressible Navier-Stokes solver for large-eddy simulation of turbulent flows," *International Journal of Numerical Methods in Fluids*, pp. 983-1017.
- [6] Genin, F., and Menon, S., 2010, "Studies of shock/turbulent shear layer interaction using Large-Eddy Simulation," *Computers & Fluids*, **39**(5), pp. 800-819.
- [7] Grady, N. R., Pitz, R. W., Carter, C. D., Hsu, K.-Y., Ghodke, C., and Menon, S., 2011, "Supersonic flow over a ramped-wall cavity flameholder with an upstream strut," (Accepted to) *Journal of Propulsion and Power*.
- [8] Maurice, M. S., 1992, "Laser velocimetry seed particles within compressible, vortical flows," *AIAA Journal*, **30**(2), pp. 376-383.
- [9] Pitz, R. W., Lahr, M. D., Douglas, Z. W., Wehrmeyer, J. A., Hu, S. T., Carter, C. D., Hsu, K. Y., Lum, C., and Koochesfahani, M. M., 2005, "Hydroxyl tagging velocimetry in a supersonic flow over a cavity," *Applied Optics*, **44**(31), pp. 6692-6700.
- [10] Grady, N. R., 2010, "Hydroxyl tagging velocimetry in a supersonic flow over a ramped-wall cavity flameholder with an upstream strut," Master's Thesis, Vanderbilt University, Department of Mechanical Engineering, Nashville, TN.
- [11] Lahr, M. D., Pitz, R. W., Douglas, Z. W., and Carter, C. D., 2010, "Hydroxyl-tagging-velocimetry measurements of a supersonic flow over a cavity," *Journal of Propulsion and Power*, **26**(4), pp. 790-797.
- [12] Ribarov, L. A., Wehrmeyer, J. A., Pitz, R. W., and Yetter, R. A., 2002, "Hydroxyl tagging velocimetry (HTV) in experimental air flows," *Applied Physics B-Lasers and Optics*, **74**(2), pp. 175-183.
- [13] Ribarov, L. A., Wehrmeyer, J. A., Hu, S., and Pitz, R. W., 2004, "Multiline hydroxyl tagging velocimetry measurements in reacting and nonreacting experimental flows," *Experiments in Fluids*, **37**(1), pp. 65-74.
- [14] Ribarov, L. A., Hu, S. T., Wehrmeyer, J. A., and Pitz, R. W., 2005, "Hydroxyl tagging velocimetry method optimization: signal intensity and spectroscopy," *Applied Optics*, **44**(31), pp. 6616-6626.
- [15] Wehrmeyer, J. A., Ribarov, L. A., Oguss, D. A., and Pitz, R. W., 1999, "Flame flow tagging velocimetry with 193-nm H₂O photodissociation," *Applied Optics*, **38**(33), pp. 6912-6917.
- [16] Pitz, R. W., Wehrmeyer, J. A., Ribarov, L. A., Oguss, D. A., Batliwala, F., DeBarber, P. A., Deusch, S., and Dimotakis, P. E., 2000, "Unseeded molecular flow tagging in cold and hot flows using ozone and hydroxyl tagging velocimetry," *Measurement Science & Technology*, **11**(9), pp. 1259-1271.
- [17] O'Byrne, S., Danehy, P. M., Tedder, S. A., and Cutler, A. D., 2007, "Dual-pump coherent anti-Stokes Raman scattering measurements in a supersonic combustor," *AIAA Journal*, **45**(4), pp. 922-933.

- [18] Hancock, R. D., Schauer, F. R., Lucht, R. P., and Farrow, R. L., 1997, "Dual-pump coherent anti-Stokes Raman scattering measurements of nitrogen and oxygen in a laminar jet diffusion flame," *Applied Optics*, **36**(15), pp. 3217-3226.
- [19] Lucht, R. P., Velur-Natarajan, V., Carter, C. D., Grinstead, K. D., Gord, J. R., Danehy, P. M., Fiechtner, G. J., and Farrow, R. L., 2003, "Dual-pump coherent anti-Stokes Raman scattering temperature and CO₂ concentration measurements," *AIAA Journal*, **41**(4), pp. 679-686.
- [20] Barlow, R. S., Carter, C. D., and Pitz, R. W., 2002, "Multiscalar Diagnostics in Turbulent Flames," *Applied Combustion Diagnostics*, K. Kohse-Hoeinghaus, and J. B. Jeffries, eds., Taylor and Francis, New York, pp. 384-407.
- [21] Nandula, S. P., Brown, T. M., Pitz, R. W., and Debarber, P. A., 1994, "Single-pulse, simultaneous multipoint multispecies Raman measurements in turbulent nonpremixed jet flames," *Optics Letters*, **19**(6), pp. 414-416.
- [22] Cheng, T. S., Yuan, T., Chao, Y. C., Lu, C. C., and Wu, D. C., 1998, "Premixed methane-air flame spectra measurements using UV Raman scattering," *Combustion Science and Technology*, **135**(1-6), pp. 65-84.
- [23] Mansour, M. S., Chen, Y. C., and Peters, N., 1999, "Highly strained turbulent rich methane flames stabilized by hot combustion products," *Combustion and Flame*, **116**(1-2), pp. 136-153.
- [24] Cheng, T. S., Wehrmeyer, J. A., Pitz, R. W., Jarrett, O., and Northam, G. B., 1994, "Raman measurement of mixing and finite-rate chemistry in a supersonic hydrogen-air diffusion flame," *Combustion and Flame*, **99**(1), pp. 157-173.
- [25] Gruber, M. R., and Nejad, A. S., 1995, "New supersonic combustion research facility," *Journal of Propulsion and Power*, **11**(5), pp. 1080-1083.
- [26] Hsu, K.-Y., Carter, C. D., Gruber, M. R., and Barhorst, T., 2007, "Experimental study of cavity-strut combustion in supersonic flow," 43rd AIAA/ASME/SAE/ASEE Joint Propulsion Conference and Exhibit, AIAA, Cincinnati, OH, AIAA-2007-5394.
- [27] Ramsey, M. C., and Pitz, R. W., 2011, "Template matching for improved accuracy in molecular tagging velocimetry," *Experiments in Fluids*, **51**(3), pp. 811-819.
- [28] Sankaran, V., and Menon, S., 2005, "LES of scalar mixing in supersonic mixing layers," *Proceedings of the Combustion Institute*, **30**, pp. 2835-2842.
- [29] El-Asrag, H., and Menon, S., 2007, "Large eddy simulation of bluff-body stabilized swirling non-premixed flames," *Proceedings of the Combustion Institute*, **31**, pp. 1747-1754.
- [30] Patel, N., and Menon, S., 2008, "Simulation of spray-turbulence-flame interactions in a lean direct injection combustor," *Combustion and Flame*, **153**(1-2), pp. 228-257.
- [31] Genin, F., and Menon, S., 2010, "Dynamics of sonic jet injection into supersonic crossflow," *Journal of Turbulence*, **11**(4), pp. 1-30.
- [32] Kim, W.-W., and Menon, S., 1999, "A new incompressible solver for Large-Eddy Simulations," *International Journal of Numerical Methods in Fluids*, pp. 983-1017.
- [33] Ghodke, C. D., Choi, J. J., Srinivasan, S., and Menon, S., "Large eddy simulation of supersonic combustion in a cavity-strut flameholder," 49th AIAA Aerospace Sciences Meeting, Orlando, Florida, January 4-7, 2011, AIAA 2011-323.
- [34] Edwards, J. R., 2008, "Numerical simulations of shock/boundary layer interactions using time-dependent modeling techniques: A survey of recent results," *Progress in Aerospace Sciences*, **44**(6), pp. 447-465.

- [35] Grady, N. R., Friedlander, T., Pitz, R. W., Carter, C. D., and Hsu, K.-Y., "Hydroxyl tagging velocimetry in a supersonic flow over a piloted cavity," 48th AIAA Aerospace Sciences Meeting, Orlando, Florida, January 4-7, 2010, AIAA-2010-1405.
- [36] Gruber, M. R., Donbar, J. M., Carter, C. D., and Hsu, K. Y., 2004, "Mixing and combustion studies using cavity-based flameholders in a supersonic flow," *Journal of Propulsion and Power*, **20**(5), pp. 769-778.
- [37] Hsu, K. Y., Carter, C. D., Gruber, M. R., Barhorst, T., and Smith, S., 2010, "Experimental study of cavity-strut combustion in supersonic flow," *Journal of Propulsion and Power*, **26**(6), pp. 1237-1246.
- [38] Bilger, R. W., 1988, "The structure of turbulent nonpremixed flames," *Twenty-Second Symposium (International) on Combustion*, The Combustion Institute, Pittsburgh, PA, pp. 475-488.
- [39] Sen, B. A., and Menon, S., 2009, "Turbulent premixed flame modeling using artificial neural networks based chemical kinetics," *Proceedings of the Combustion Institute*, 32, pp. 1605-1611.

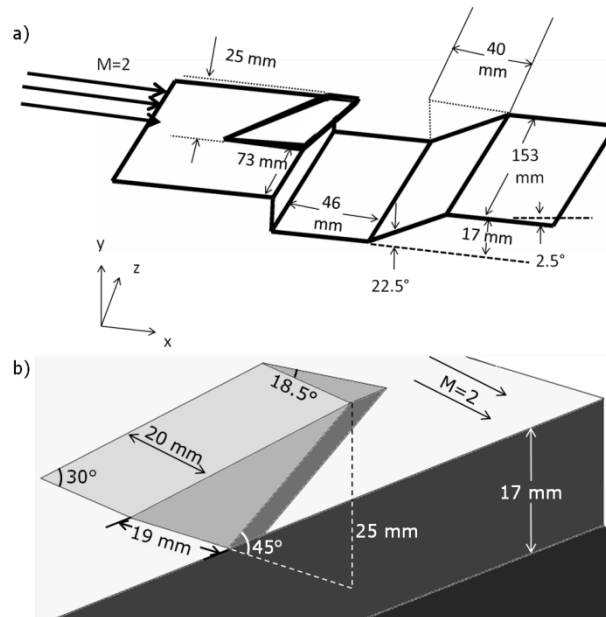


Fig. 1. Mach 2 flow in Research Cell 19 at WPAFB with a piloted ramped cavity and strut (a), and a close up of the strut (b).

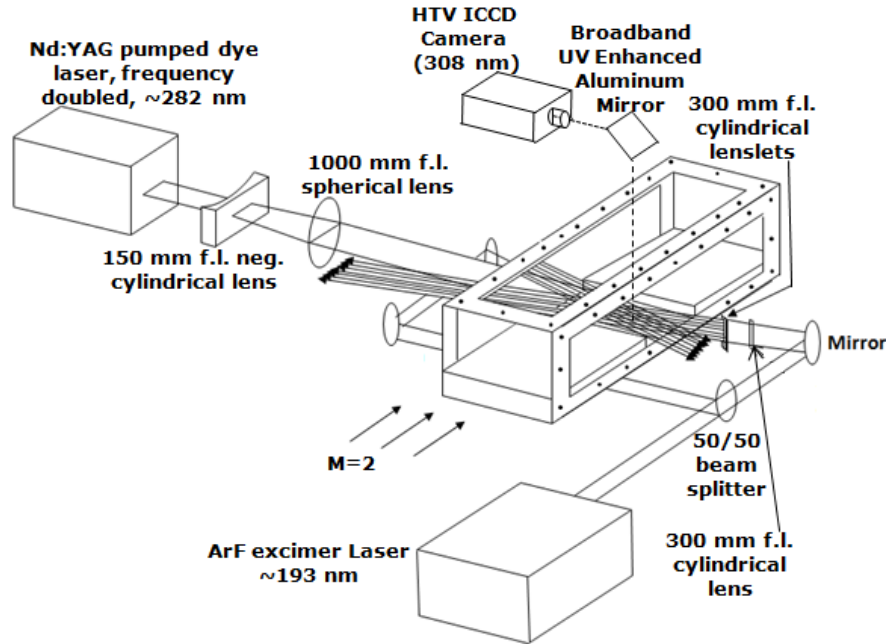


Fig. 2. Schematic of the hydroxyl tagging velocimetry (HTV) experimental system in Research Cell 19 at WPAFB.

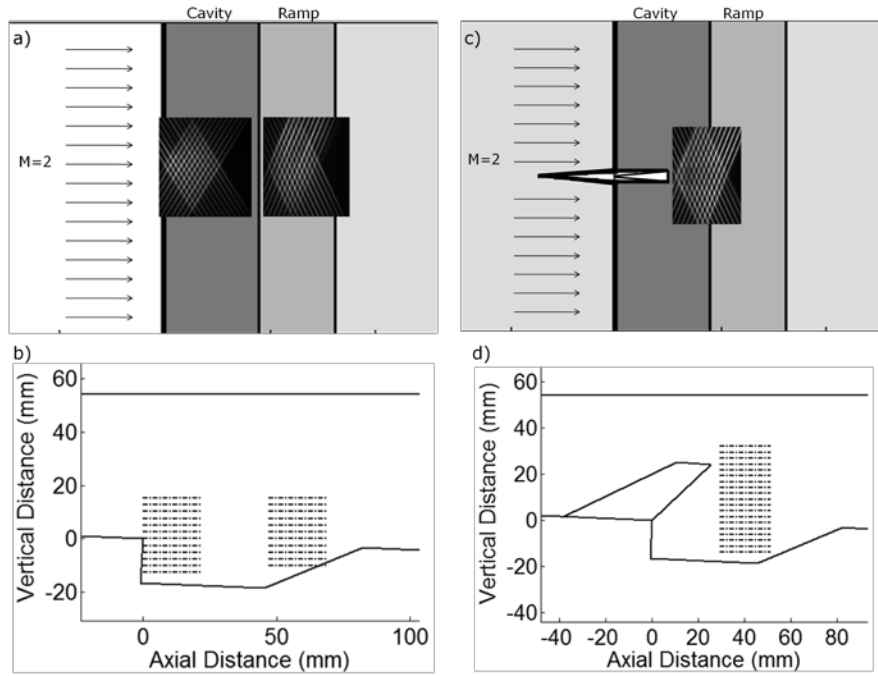


Fig. 3. Schematic of the cavity showing the overhead and side view positions of the HTV grid for the *no-strut* configuration a) and b) and for the *strut* configuration c) and d).

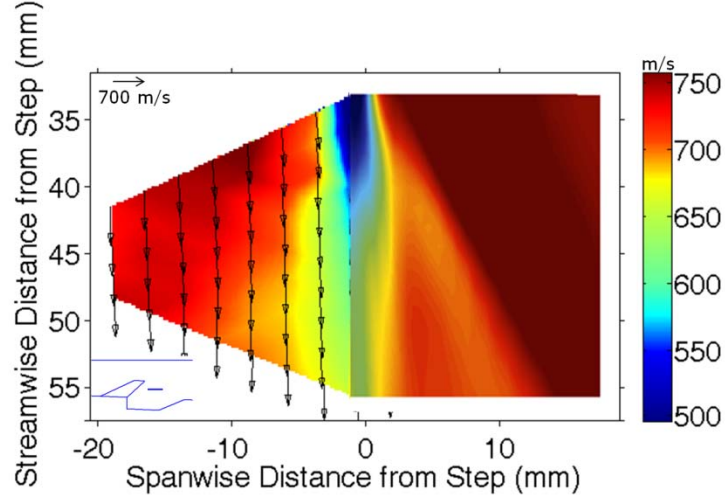


Fig. 4. Side-by-side comparison of 300 shot experimental (left) and LES predictions (right) of streamwise average velocity at $y=12.7$ mm for the *strut* configuration. The LES predictions are at the same location as the experimental data and subsequently flipped across the centerline for direct comparison. Arrows in the experimental data indicate the 2D velocity.

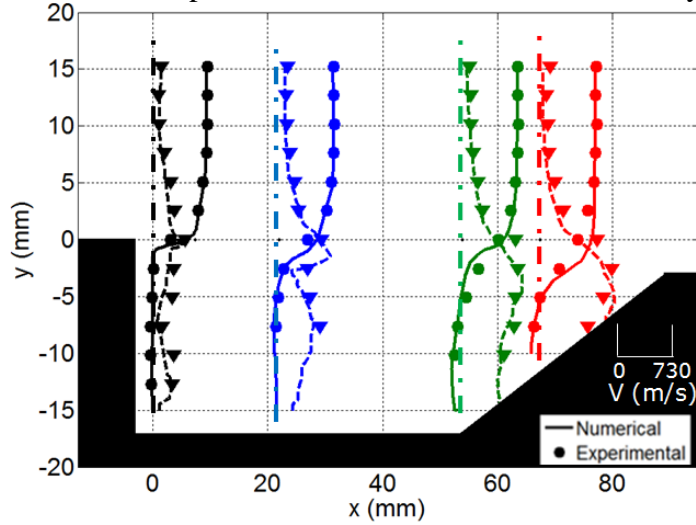


Fig. 5. Mean streamwise velocity (solid lines, points) and RMS fluctuation (dashed lines, triangles) profiles along the centerline plane for the no-strut configuration. The cavity overlay has been adjusted for data clarity.

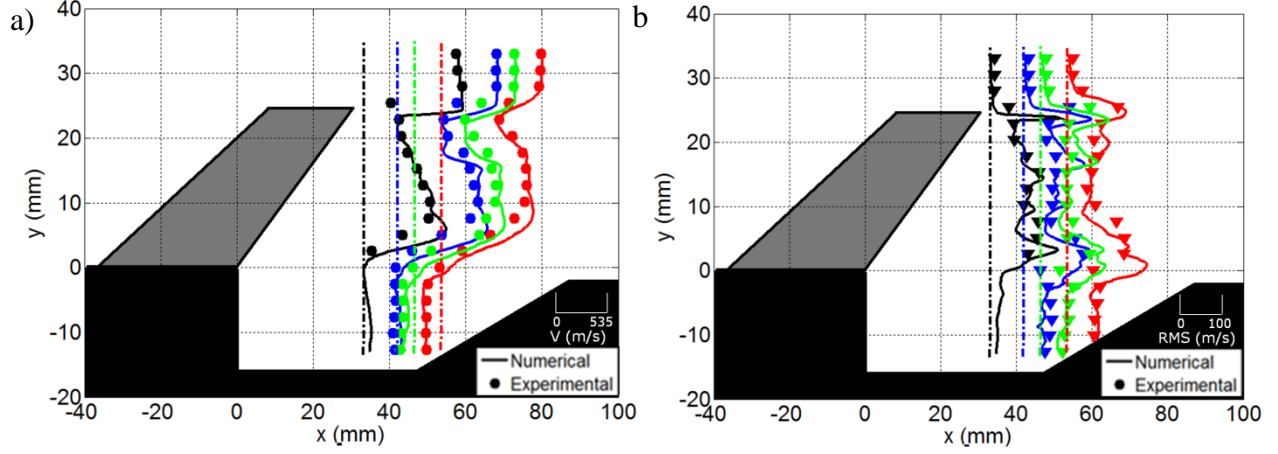


Fig. 6. Profiles of (a) mean streamwise velocity and (b) RMS fluctuation along the centerline plane for the strut configuration.

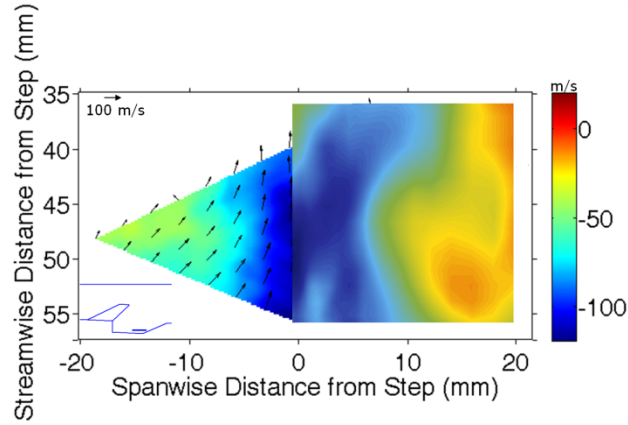


Fig. 7. Side-by-side comparison of 300 shot experimental (left) and LES predictions (right) of streamwise average velocity at $y = -12.7$ mm for the *strut* configuration. The LES predictions are at the same location as the experimental data and subsequently flipped across the centerline for direct comparison. Arrows in the experimental data indicate the 2D velocity.

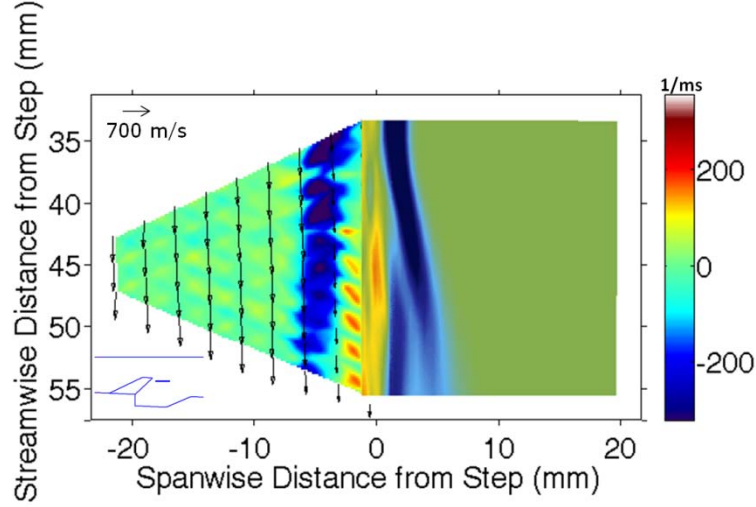


Fig. 8. Side-by-side comparison of 300 shot experimental (left) and LES predictions (right) of y -component average vorticity at $y = 20.3$ mm for the *strut* configuration. The LES predictions are at the same location as the experimental data and subsequently flipped across the centerline for direct comparison. Arrows in the experimental data indicate the 2D velocity.

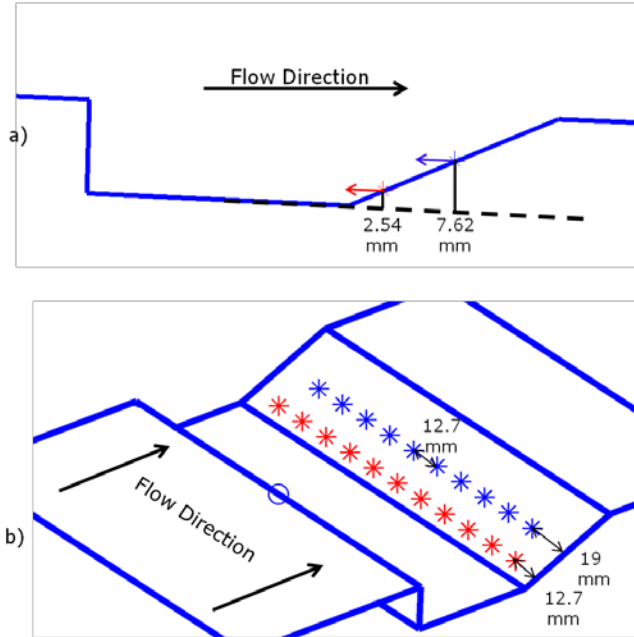


Fig. 9. Close up of the fuel (red stars) and air (blue stars) injectors from the side (a) and from above at an angle (b). Each row of injectors has 12.7 mm spacing with 11 fuel injectors and 10 air injectors. The exit diameter of the injectors is 1.98 mm and 1.59 mm for the fuel and air injectors respectively.

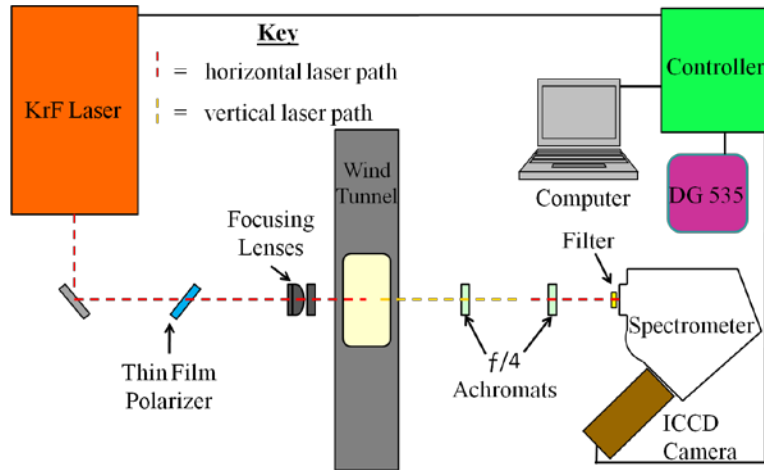


Fig. 10. Schematic of the UV Raman experimental system in Research Cell 19 at WPAFB

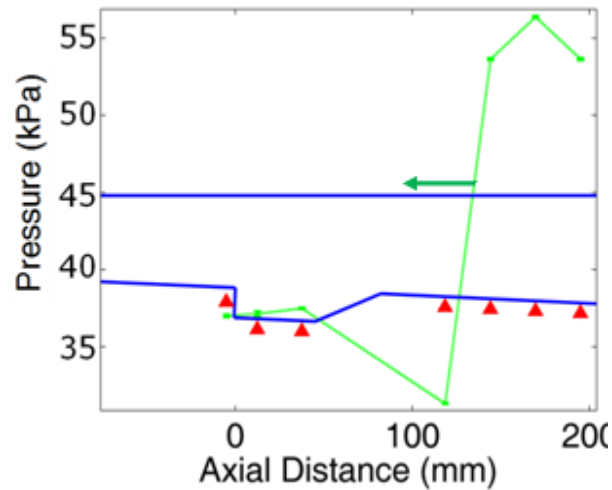


Fig. 11. Example mean wall pressure data and the standard deviation of the 1 Hz measurement was generally $<1\%$. Insert shows the pressure port locations (solid triangles) with respect to the cavity.

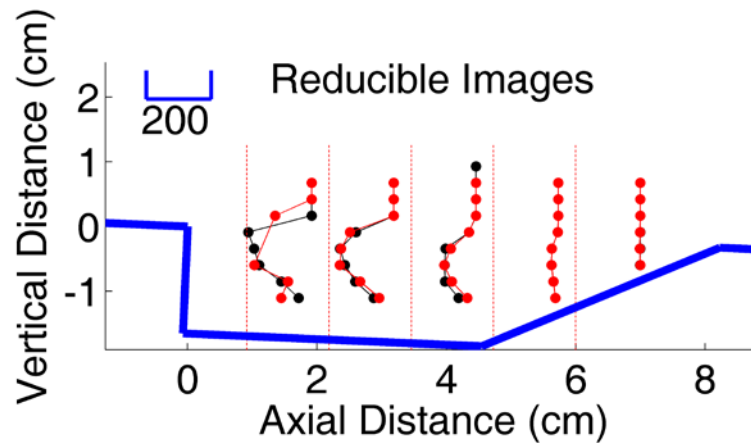


Fig. 12. Number of reducible images for no secondary air (black dots) and secondary air (red dots).

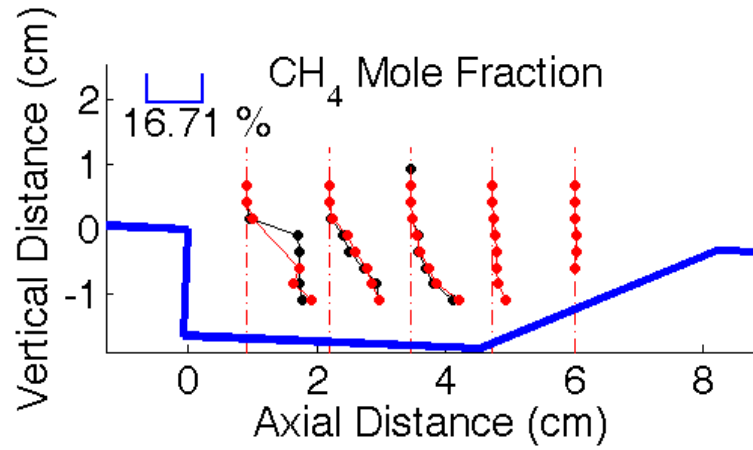


Fig. 13. Time averaged methane mole fraction for no secondary air (black dots) and secondary air (red dots).

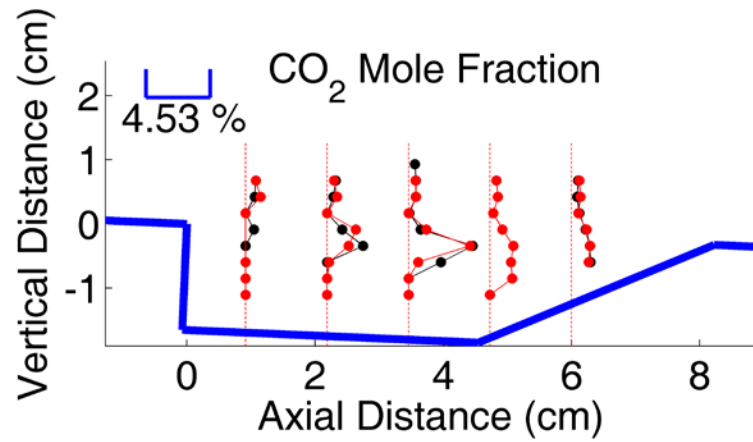


Fig. 14. Time averaged carbon dioxide mole fraction for no secondary air (black dots) and secondary air (red dots).

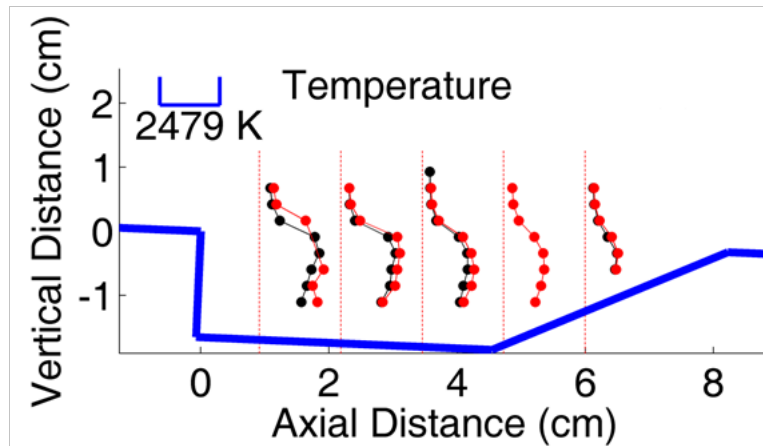


Fig. 15. Time averaged temperature for no secondary air (black dots) and secondary air (red dots).

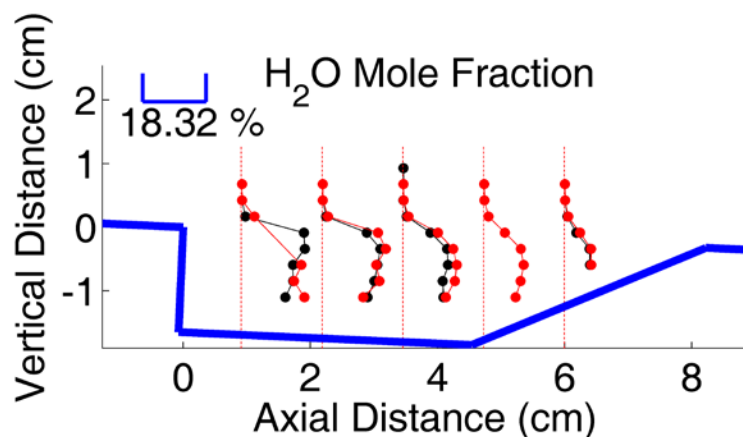


Fig. 16. Time averaged water mole fraction for no secondary air (black dots) and secondary air (red dots).

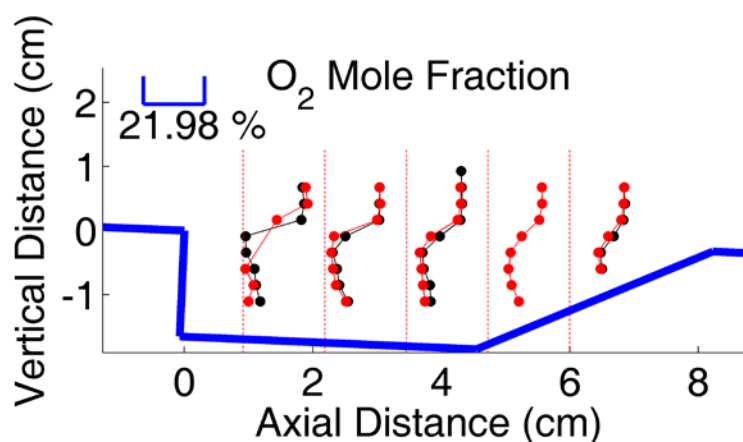


Fig. 17. Time averaged oxygen mole fraction for no secondary air (black dots) and secondary air (red dots).

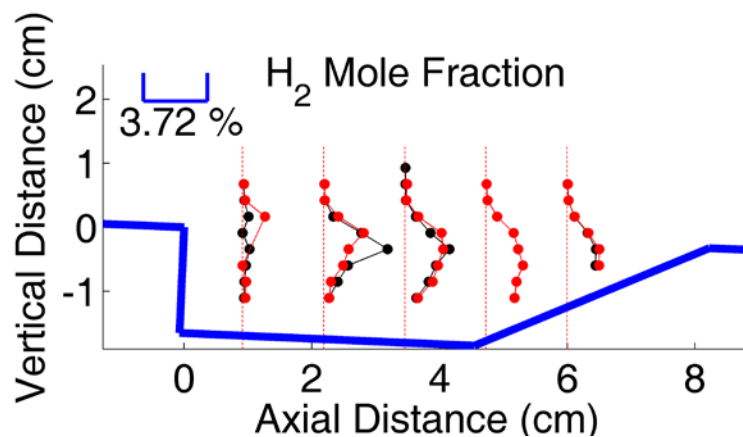


Fig. 18. Time averaged hydrogen mole fraction for no secondary air (black dots) and secondary air (red dots).

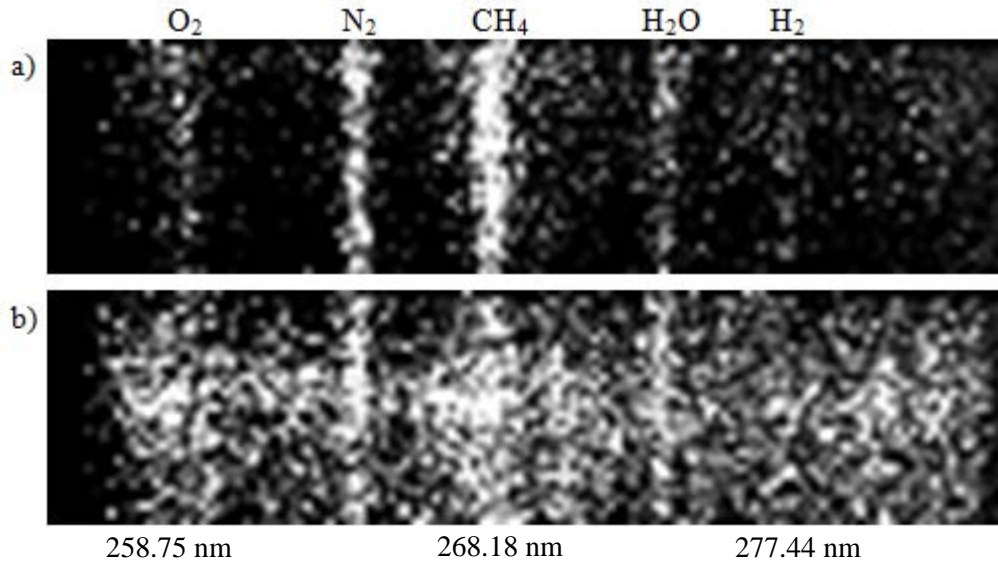


Fig. 19. Raman spectra taken inside the combustor showing a) a reducible image, and b) an irreducible image due to broadband interference during combustion with no secondary air injection both taken at $x = 0.92$ cm and $y = 0.85$ cm.

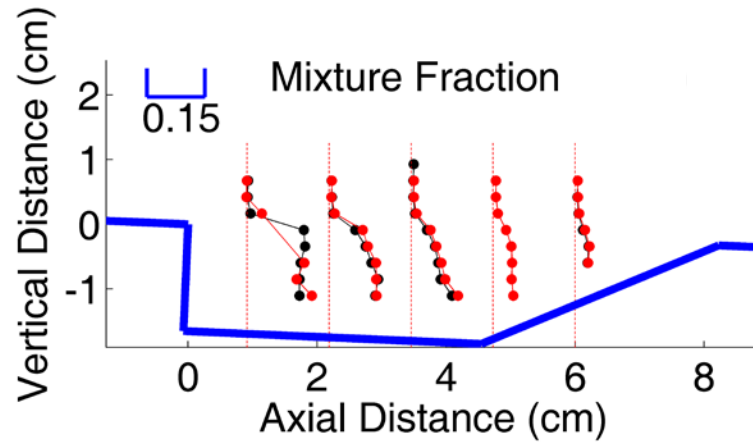


Fig. 20. Time averaged mixture fraction for no secondary air (black dots) and secondary air (red dots).

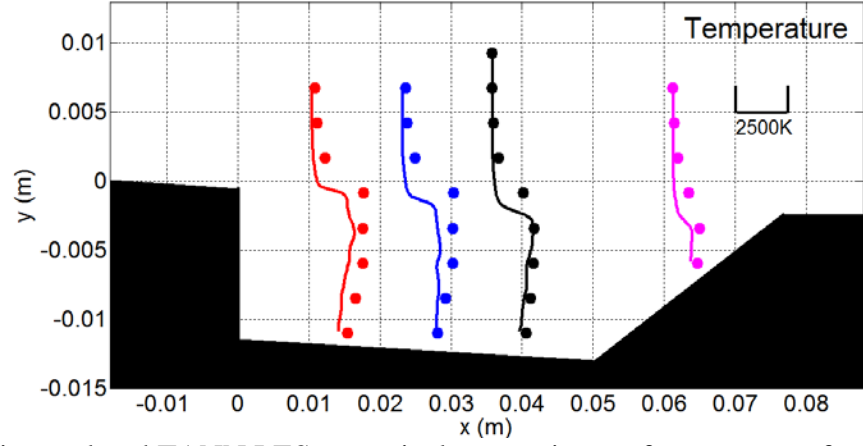


Fig. 21. Experimental and TANN LES numerical comparisons of temperature for 102 SLPM of fuel.

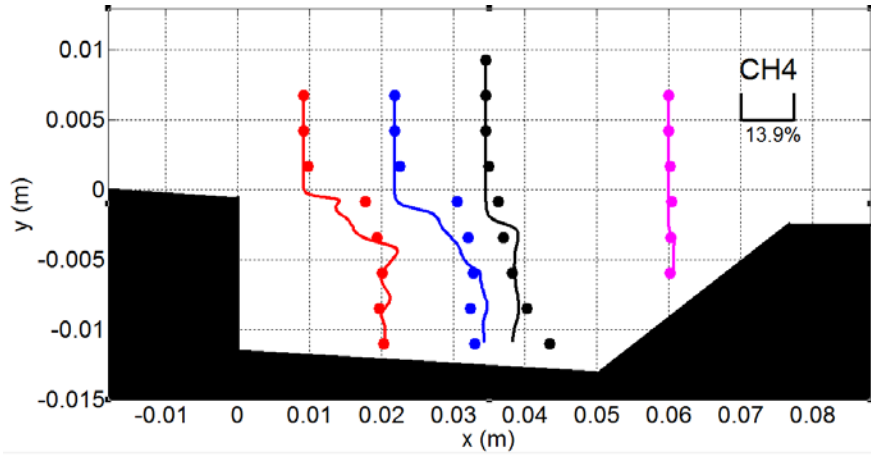


Fig. 22. Experimental and TANN LES numerical comparisons of CH_4 for 102 SLPM of fuel.

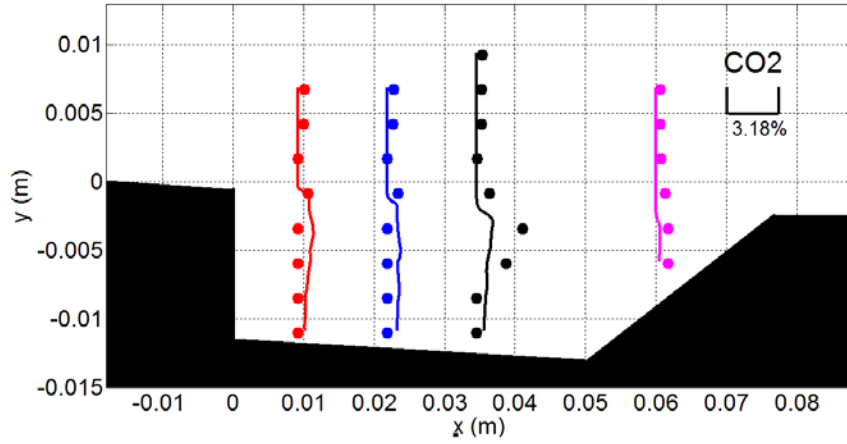


Fig. 23. Experimental and TANN LES numerical comparisons of CO_2 for 102 SLPM of fuel.

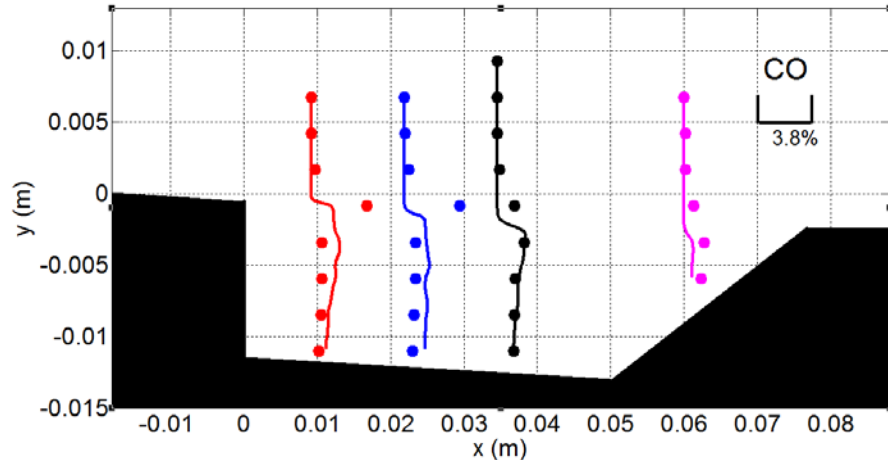


Fig. 24. Experimental and TANN LES numerical comparisons of CO for 102 SLPM of fuel.

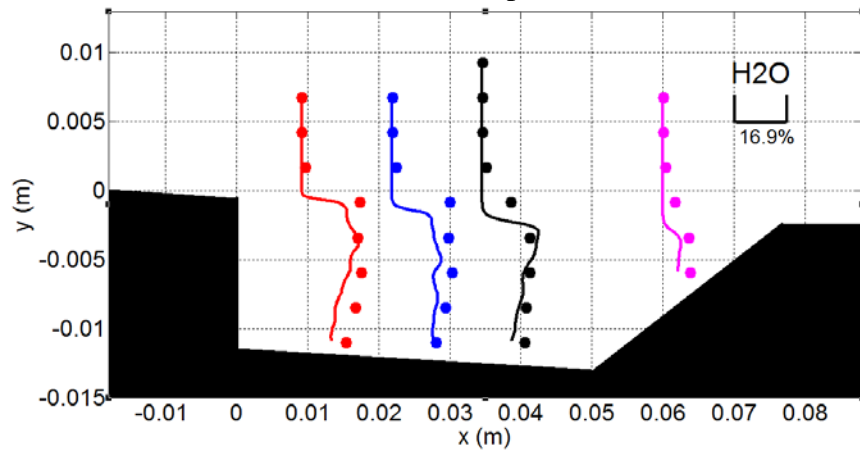


Fig. 25. Experimental and TANN LES numerical comparisons of H_2O for 102 SLPM of fuel.